ACS APPLIED BIO MATERIALS

Article

Sensitive Chronocoulometric Detection of miRNA at Screen-printed Electrodes modified by gold decorated MoS2 Nanosheets

Abhijit Ganguly, John Benson, and Pagona Papakonstantinou

ACS Appl. Bio Mater., **Just Accepted Manuscript** • DOI: 10.1021/acsabm.8b00398 • Publication Date (Web): 10 Sep 2018

ACS Publications

is published by the American Chemical Society. 1155 Sixteenth Street N.W., Washington, DC 20036

Sensitive Chronocoulometric Detection of miRNA at Screen-printed Electrodes modified by Gold decorated MoS_2 Nanosheets

Abhijit Ganguly,[†] *John Benson,*[‡] *and Pagona Papakonstantinou*[*,†]

[†]School of Engineering, Engineering Research Institute, Ulster University, Newtownabbey BT37 0QB, United Kingdom

[‡]2-DTech, Core Technology Facility, 46 Grafton St., Manchester M13 9NT, United Kingdom

[*]Corresponding author, e mail address: *p.papakonstantinou@ulster.ac.uk*

KEYWORDS. *Molybdenum disulfide (MoS_2) Nanosheets, Ionic Liquid Assisted Grinding Exfoliation, Gold Decorated MoS_2 Hybrid Nanosheets, Screen-Printed Gold Electrodes, Electrochemical Deposition, microRNA-21 (miRNA-21), Electrochemical microRNA-sensor, Chronocoulometric Detection*

ABSTRACT: Developing novel simple and ultrasensitive strategies for detecting microRNAs (miRNAs) is highly desirable because of their association with early cancer diagnostic and prognostic processes. Here a new chronocoulometric sensor, based on semiconducting 2H MoS_2 nanosheets (MoS_2 NSs) decorated with a controlled density of monodispersed small gold nanoparticles (AuNPs@MoS_2), was fabricated via electrodeposition, for the highly sensitive detection of miRNA-21. The size and interparticle spacing of AuNPs was optimized by controlling nucleation and growth rates through tuning of deposition-potential and Au-precursor concentration and by getting simultaneous feedback from morphological and electrochemical activity studies. The sensing strategy, involved the selective immobilization of thiolated capture probe DNA (**CP**) at AuNPs and hybridization of **CP** to a part of miRNA target, whereas the remaining part of the target was complementary to a signaling non-labelled DNA sequence that served to amplify the target upon hybridization. Chronocoulometry provided precise quantification of nucleic acids at each step of the sensor assay by interrogating $[Ru(NH_3)_6]^{3+}$ electrostatically bound to phosphate backbones of oligonucleotides. A detailed and systematic optimization study demonstrated that the thinnest and smallest MoS_2 NSs improved the sensitivity of the AuNP@MoS_2 sensor achieving an impressive detection limit of ≈100 aM, which is 2 orders of magnitude lower than that of bare Au electrode and also enhanced the DNA-miRNA hybridization efficiency by 25%. Such improved performance can be attributed to the controlled packing density of **CP**s achieved by their self -assembly on AuNPs, large interparticle density, small size and the intimate coupling between AuNPs and MoS_2. Alongside the outstanding sensitivity, the sensor exhibited excellent selectivity down to femtomolar concentrations, for discriminating complementary miRNA-21 target in a complex system composed of different foreign targets including mismatched and non-complementary miRNA-

155. These advantages make our sensor a promising contender in the point of care miRNA sensor family for medical diagnostics.

▪ INTRODUCTION

Micro RNAs (miRNAs) is a class of short (about ~19–23 nucleotides) single-stranded non-coding RNAs that regulate gene expression and cellular processes.[1-3] Studies have demonstrated that abnormality in miRNA expression is closely related to initiation and progression of cancers. For example, overexpressed circulating level of miRNA-21 was considerably higher in plasma specimens of patients suffering from breast, cervical, lung or pancreatic cancer compared to healthy controls. As a result, miRNA-21 has become one of the clinically important diagnostic biomarkers for cancer screening and disease progression.[1] However, the relatively low level of miRNAs expression, their small size and their inherent degradable nature make direct quantification particularly challenging, necessitating the development of new platforms for their accurate and straightforward quantification in clinical samples. Among these, electrochemical-based platforms hold promise, due to their advantages of fast analysis, cost-effectiveness, and simplicity of operation.

It is well established that, the physical structure of a DNA probe layer immobilized on the electrode surface is critical in defining the overall performance of the sensor in terms of selectivity, sensitivity and reproducibility. Although the self-assembly of thiolated DNA at the surface of a gold electrode, exploiting the well-established Au-S chemistry, is a widely employed immobilisation approach,[4-5] it remains challenging to precisely control the orientation and conformation of surface-tethered oligonucleotides and finely tune the hybridization efficiency. Theoretical studies employing thiolated DNA on gold flat surfaces have predicted that efficient hybridization occurs with large inter-probe distances and upright conformations;[4-6] densely packed probe surfaces should be avoided as they restrict the accessibility of target DNA molecules due to steric effects.[5-6] In practice, the assembly of DNA is influenced by several factors including interactions between nitrogen atoms of DNA bases and the Au surface. Intuitively one would expect that, the surface coverage of DNA-probe recognition layer can be regulated through a controlled gold nanoparticle (AuNP) distribution of small particle size, narrow size variation and appropriate particle separation, instead of employing flat gold surfaces, with multiple anchoring points. Our work verifies this hypothesis, by controlling the size and interparticle spacing of AuNPs through judicious choice of electrodeposition conditions and by getting simultaneous feedback from morphological and electrochemical activity studies.

Molybdenum disulfide (MoS_2) is an important member of transition-metal dichalcogenides (TMDC), with unique layered structure, consisting of a single layer of Mo atoms sandwiched between two layers of S atoms in a trigonal prismatic arrangement. The weak Van der Waals interactions between the MoS_2 sheets make it possible to exfoliate the bulk MoS_2 to a few-layers or even to a single-layer crystalline sheet, via mechanical,[7-8] chemical routes or a combination of both.[9-14] The decoration of a few-layer MoS_2 nanosheets (MoS_2 NSs) with noble metal nanoparticles (NPs), such as Au, Ag, Pt, has become a popular and effective way to functionalize the 2D MoS_2-surface and enhance its sensing performance.[2-3, 14-18] So far, the application of MoS_2 or gold decorated MoS_2 NSs (AuNPs@MoS_2 NSs) for miRNA-21 detection is limited to a few studies, mainly classified to fluorescence-quenching,[12-13, 19-21] surface-enhanced Raman scattering,[17] and electrochemical[2-3, 15] based detection methods. Interestingly, in most of the previous studies on AuNPs@MoS_2 hybrids,[2-3, 11, 17-18, 22] the MoS_2 NSs were exfoliated via the popular lithium intercalation route.[9] This exfoliation approach results in MoS_2 layers of metallic phase, with a high population of defects in the basal plane,[11, 18, 23] which can act either as nucleation sites for the growth of high density of AuNPs with a large variance in particle size or as anchoring sites for non-specific adsorption. Uncontrolled AuNP growth on MoS_2 NSs is a limitation for its use in nucleic acid sensing, as it favors a highly packed assembly of DNA probe immobilization, which restricts the accessibility of target molecules. Sonication of bulk single crystals in appropriate solvents provides MoS_2 NS of semiconducting 2H phase.[12, 14, 16, 21, 24] However, their decoration with AuNPs via chemical reaction routes is limited at the edges, due to the absence of defects in the basal plane, restricting dramatically their use.[16, 25] Hence, alternative methods for the controlled synthesis of AuNPs on defect free MoS_2 NSs should be sought; however this area is an almost unexplored terrain. In this contribution, we show that these requirements can be met under well controlled electrochemical deposition (ECD) conditions.[15, 26-31] ECD is also free of critical drawbacks such as the formation of “free” AuNPs, which usually coexist with AuNPs@MoS_2 hybrids in solution-based routes.[11, 22, 24, 32-33]

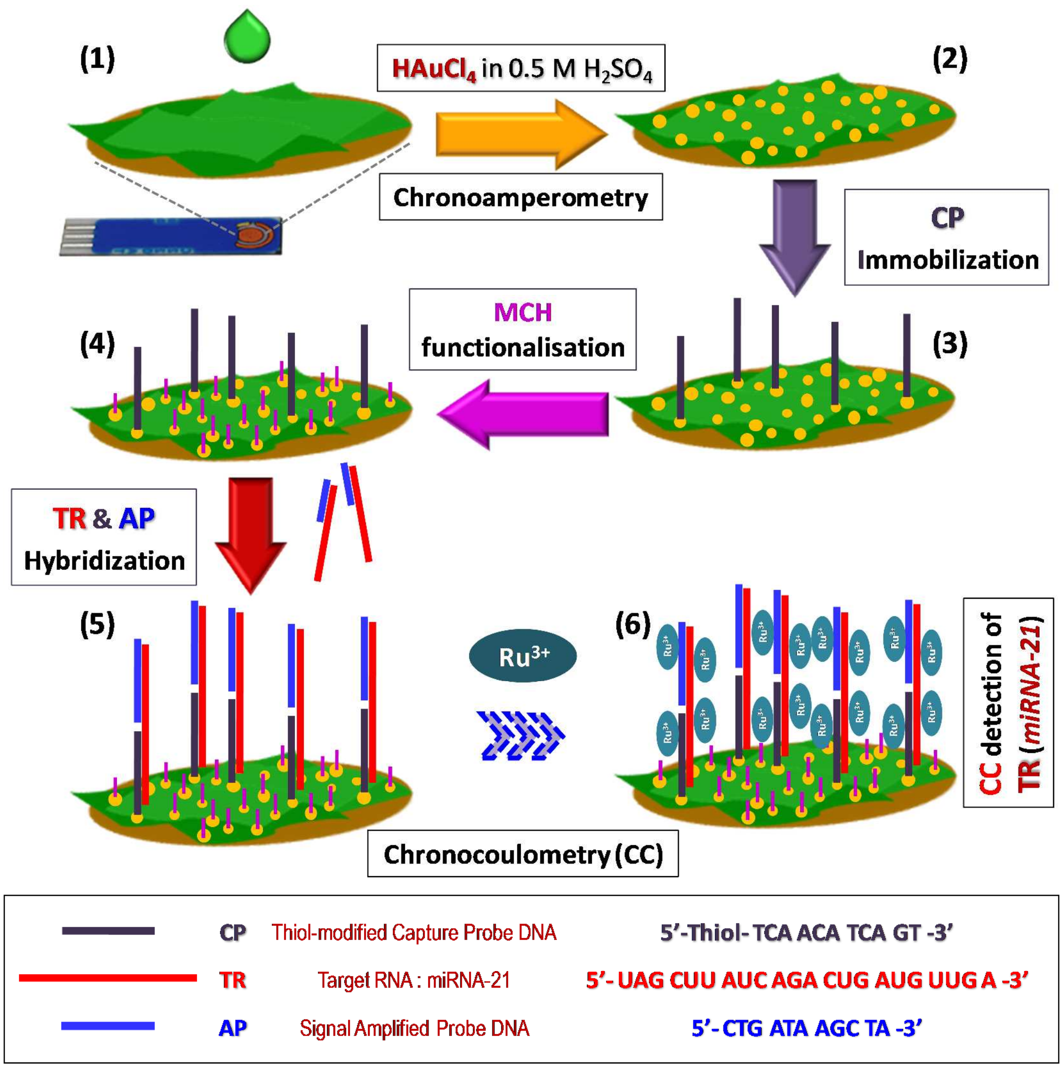

Figure 1. Fabrication of miRNA-21 sensor and detection strategy. Coating of MoS_2 nanosheets (MoS_2 NSs) on commercial screen-printed gold electrodes (SPGEs) (1); decoration of MoS_2 NSs with AuNPs (to create AuNPs@MoS_2 NSs) following an optimized chronoamperometric (CA) route (2); assembly of ssDNA capture probe: anti-miRNA-21 (**CP**), miRNA-21 target (**TR**) and signal amplification probe (**AP**) on AuNPs@MoS_2/SPGE sensor (3-5); chronocoulometric (CC) detection of miRNA (**TR**) by monitoring $[Ru(NH_3)_6]^{3+}$ (RuHex) electrostatically bound to phosphate backbones of oligonucleotides (6).

Herein, we report a simple and sensitive electrochemical platform for miRNA-21 detection using a screen-printed gold electrode (SPGE) modified with MoS_2 NSs decorated with a controlled density of monodispersed AuNPs (AuNPs@MoS_2 NSs) achieved by chronoamperometric (CA) electrodeposition. Utilizing SPGPE as a base platform offers the possibility of building a portable and disposable miniaturized electrode system suitable for both electrodeposition of AuNPs and subsequent bio-functionalization, for laboratory and onsite-clinical-measurements. Figure 1 illustrates schematically the fabrication of the sensor and the detection strategy (described in the *Supporting Information* (SI), Section S2), which involves selective immobilisation of thiolated capture probe ssDNA (**CP**) at AuNPs@MoS_2 and hybridisation of the immobilized **CP** to a part of miRNA target (**TR**), whereas the remaining part of **TR** is complementary to a ssDNA sequence (**AP**; Amplification Probe) that serves to amplify the hybridization signal (Table S1). We employ chronocoulometry to quantify the amount of nucleic acids at each step of the detection strategy by monitoring $[Ru(NH_3)_6]^{3+}$ (RuHex) electrostatically bound to phosphate backbones of DNA or DNA-RNA hybrids. A detailed optimization study on both AuNP deposition and immobilization steps achieved an impressive detection limit of ~100 aM, which is 2 orders of magnitude lower than that of bare Au electrode and also enhanced the DNA-miRNA hybridization efficiency by 25%. Moreover, this newly developed biosensor was highly specific toward the target sequence miRNA-21 demonstrating the ability to differentiate between sequences that differed even by a single base, along with a clear distinction in a medium consisting of many interfering targets mixed together.

Among the electrochemical based detection routes, we have employed the chronocoulometry (CC) technique as the detection method of choice, first proposed by Steel et al.[34] Literature reports have revealed that CC can be highly effective compared to any voltammetric methods in discriminating against background contribution at relatively high potentials; hence it can be used to generate a significantly more intense signal with higher resolution.[4, 34-35] CC is a fast (hundreds of milli-seconds) and non-destructive technique, particularly useful for analytes like DNA or RNA, which are prone to degradation even in relatively mild environments. So far, the principle and employment of CC based sensing approach has been established and optimized for DNA on planar Au electrode systems.[4, 6, 34-35] The work presented here is the first study that provides a detailed account on the optimization and employment of CC technique for the detection of miRNA on semiconductor/AuNP sensor.

▪ RESULTS AND DISCUSSION

Electrochemical Deposition of Gold Nanoparticles on MoS_2 Nanosheets.

Our initial studies revealed that the electrochemical pretreatment of the MoS_2/SPGE working electrode in H_2SO_4 was crucial for achieving well-controlled reproducible AuNP deposition. (SI, Section S3, Figures S2). Similarly, it was evident from our studies that the electrodeposition process is better controlled under a static applied potential (CA route) than that under dynamic potential scan (like CV method), resulting in homogeneous distribution of small AuNPs (SI, Section S4, Figure S3). We investigated the effects of applied potential and concentration of $HAuCl_4$ solution on the CA process as described below.

Effect of Applied Potential (*V_{app}*). The applied potential, V_{app}, is considered one of the main factors that govern the Au electrodeposition process, affecting the size and monodispersity of the resultant nanoparticles. It has been established, that negative overpotentials relative to standard potential for $AuCl_4^-$ reduction to Au^0, (+0.8 V versus Ag/AgCl (sat. KCl)) favor the creation of new nucleation sites over the growth of previously created nuclei.[26-29] Figures 2(a-d) demonstrate the effect of V_{app} on the AuNPs electrodeposited on MoS_2/SPGE, when varying the V_{app} potential from +0.1 to -0.2 V. It is observed that the application of decreasing V_{app} potentials, leads gradually to a larger number of nucleation sites and hence to larger density of smaller, evenly distributed AuNPs, corroborating earlier work.[27-28]

Two growth modes are evident, depending on the V_{app} potential. For positive V_{app} values (+0.1V, 0V), the growth of a small number of initial nuclei is favored over the establishment of new nucleation sites as indicated by the large particle size and low packing density in Figures 2(a-b), consistent with earlier reports.[27-28] Statistical analysis, performed on the SEM images, presented by the particle size histogram in Figure 3a, confirms the observation. AuNPs grown at +0.1 V (least negative overpotential) result in large agglomerated particles (mean diameter, $D_m \approx$ 262 nm) with low particle density (N_D: particle number density ≈ 1.18 particles/μm^2). Notably, the large standard deviation of NP-size, (***SD*** > ±108 nm) represents an irregular size distribution of AuNPs, and the presence of aggregated Au particles.

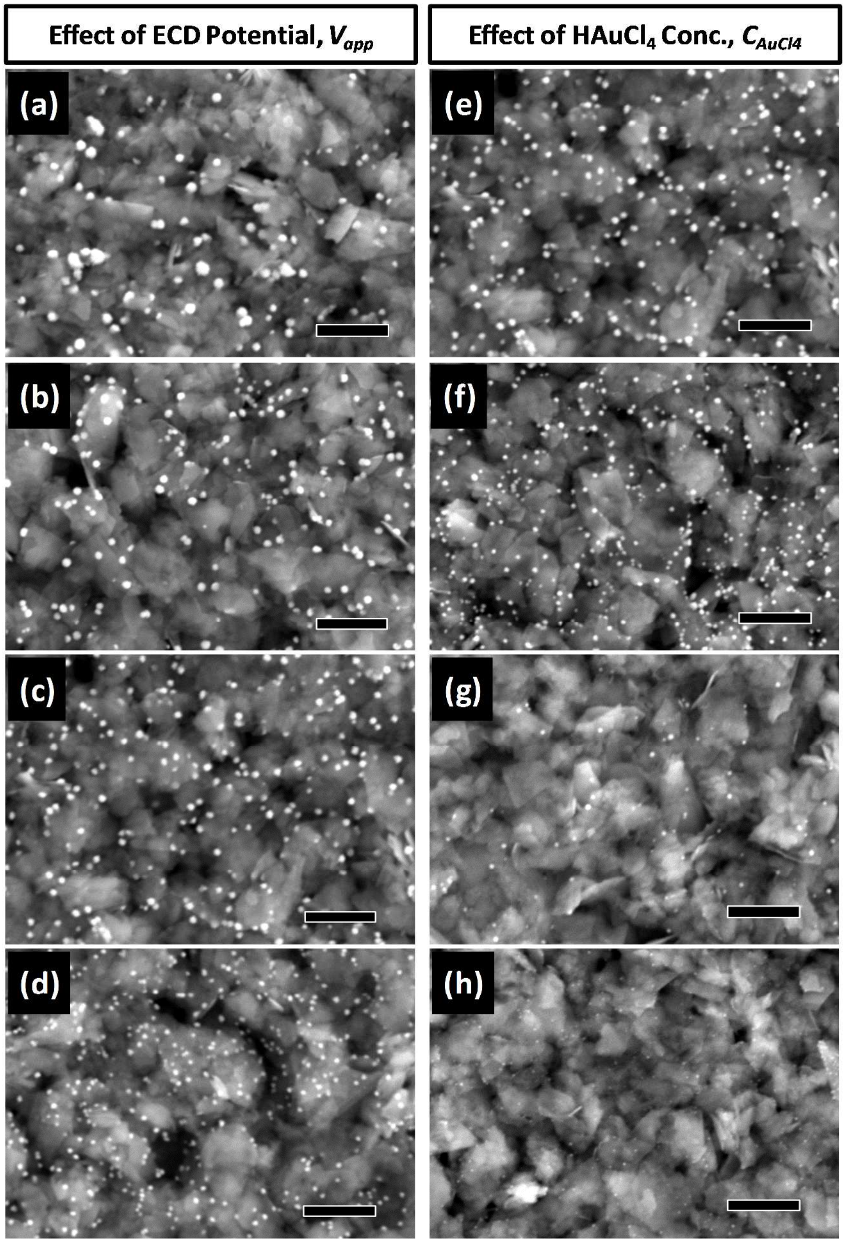

Figure 2. Morphological characterisations of AuNPs@MoS_2 hybrids. SEM images of AuNPs electrodeposited via chronoamperometry (CA) on the MoS_2/SPGEs electrodes (a-d) at different V_{app}: [(a) +0.1 V, (b) 0.0 V, (c) -0.1 V, (d) -0.2 V] with $C_{AuCl_4^-}$: 1 mM; and (e-h) at different $C_{AuCl_4^-}$: [(e) 1.0, (f) 0.5, (g) 0.1, and (h) 0.05 mM] at V_{app}: -0.1 V. V_{app}: Applied Potential,

$C_{AuCl_4^-}$: Concentration of $HAuCl_4$ in 0.5 M H_2SO_4. MoS_2 Loading: 50 μg. Potential scan-duration: 360 s. Scale bar: 1μm.

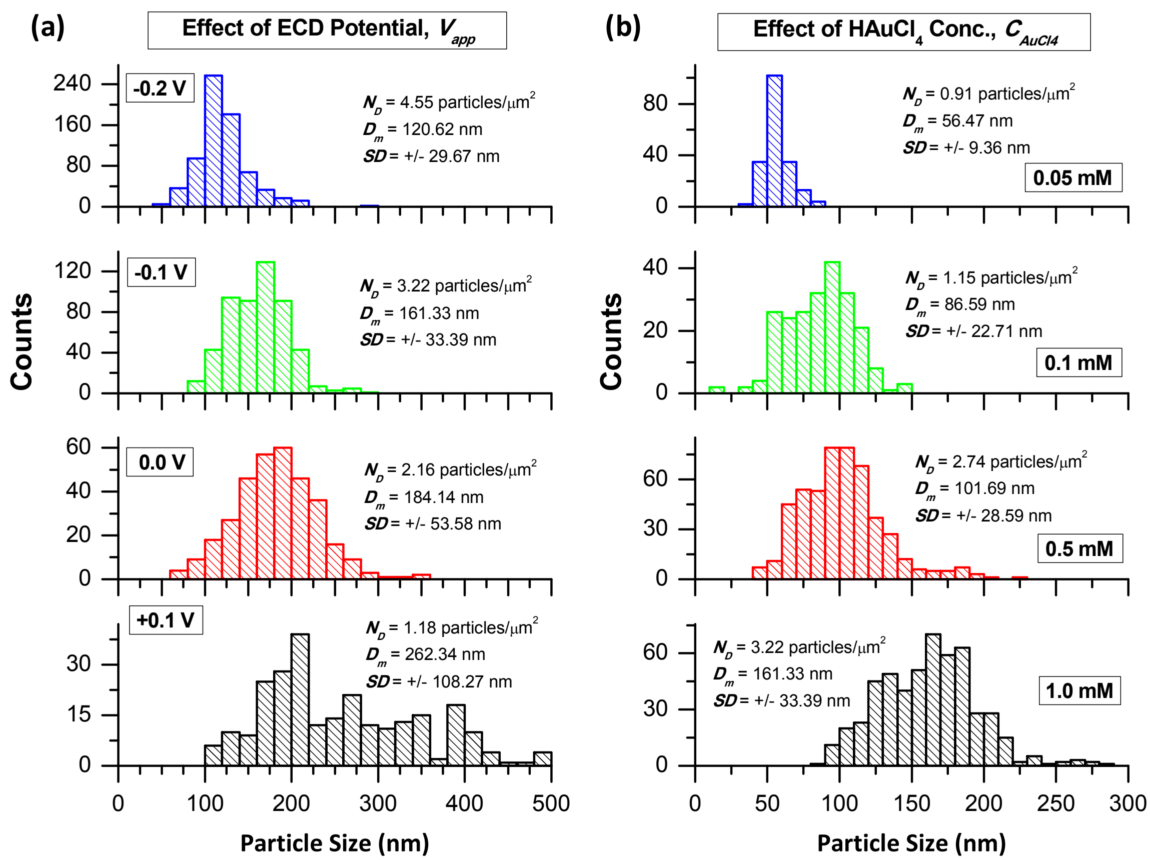

Figure 3. Statistical analysis of morphological parameters. Particle size histograms of AuNPs electrodeposited via CA on the MoS_2/SPGEs electrodes at various (a) Applied Potentials, V_{app} (with $C_{AuCl_4^-}$: 1 mM), and (b) $HAuCl_4$ Concentrations, $C_{AuCl_4^-}$: (at V_{app}: -0.1 V). Statistical analysis has been performed on at least 3~4 independent SEM images for each sample. The statistical parameters of each sample are mentioned in its respective histogram: N_D: Particle Number Density, D_m: Mean Diameter of AuNP, and SD: Standard Deviation of NP-size.

In contrast, the application of negative V_{app} values (-0.1V, -0.2V) favors instantaneous nucleation, facilitating the formation of higher density small size particles (Figures 2c-d). The particle size histogram (Figure 3a) reveals that the Au-ECD at -0.2 V could reduce the size ($D_m \approx$ 120 nm) of AuNPs by more than 2 times and improve the N_D (~4.55 particles/μm^2) by nearly 4 times. Notably, the ***SD*** value drops down to ±30 nm indicating reduced size dispersion.

On the other hand, at augmented negative potentials, such as V_{app} = -0.3 V, the $AuCl_4^- \rightarrow Au^0$ reduction rate became high enough, resulting in aggregation (SI, Section S5, Figure S5).

Effect of $HAuCl_4$ Concentration ($C_{AuCl_4^-}$). As discussed previously in order to produce a high particle density, a large negative nucleation overpotential should be applied. This results in a high nucleation density but also a fast growth rate.[30-31] Fast growth rate is problematic as it results in a rapid expansion of the diffusion zone around the growing nucleus. Diffusion zone is the area of electrolyte around the nucleus that has a reduced concentration of metal ions present compared to the bulk electrolyte, because ions are been reduced and merged into the growing nuclei. As these diffusion zones expand, adjacent zones eventually merge. Nuclei, whose diffusion zones have coupled, experience retarded growth compared to nuclei with isolated diffusion zones. As a result, diffusion zone coupling results in different growth rates, hence a range of particle sizes is being created. A large particle size distribution can result in considerable problems in terms of sensitivity and reproducibility of sensor performance. So efforts to eliminate the depletion region around each nucleus would eliminate interparticle diffusion coupling and hence allow the formation of nanoparticles with uniform size. Our strategy to keep diffusion zone coupling to a minimum involves slow growth rate via low concentrations of the gold precursor.

The radius of the depletion region around each nucleus varies proportionally with the bulk concentration of metal ions (here, $AuCl_4^-$).[26, 30-31] High concentrations of $HAuCl_4$ ($\boldsymbol{C_{AuCl_4^-}}$), give rise to fast growth rate, thereby permitting inter-particle diffusion zone coupling to occur, resulting in various size distributions. In contrast, at lower concentrations of $HAuCl_4$, growth rate of nuclei is slowed, thereby keeping diffusion zone coupling to a minimum, thus leading to the formation of smaller diameter monodisperse AuNPs.

Figures 2(e-h) demonstrate the effect of $\boldsymbol{C_{AuCl_4^-}}$ on the AuNPs electrodeposited on MoS_2/SPGE at an applied voltage of -0.1V. As $\boldsymbol{C_{AuCl_4^-}}$ decreases, SEM images display progressively smaller AuNPs with lower packing density and improved size distribution, with the best values attained at $\boldsymbol{C_{AuCl_4^-}} \approx 0.1 - 0.05$ mM (Figures 2g and 2h). The particle size histogram plots (Figure 3b) reveal that by reducing the $\boldsymbol{C_{AuCl_4^-}}$ from 1.0 to 0.05 mM, the AuNPs size ($\boldsymbol{D_m}$) reduces by nearly 3 times, while the ***SD*** value drops down to only ±9.36 nm, reflecting an improved degree of monodispersion on the resultant AuNPs.

Electrochemical Characterization of AuNPs@MoS_2 Hybrid Nanosheets. The effects of $\boldsymbol{V_{app}}$ and $\boldsymbol{C_{AuCl_4^-}}$ were further characterized (Figure 4) in order to optimize the AuNP electrodeposition strategy, by estimating two electrochemical parameters $\boldsymbol{Q_{dp}}$ and $\boldsymbol{Q_{ox}}$. Here, $\boldsymbol{Q_{dp}}$ represents the total charge involved during the Au(III) reduction to AuNPs formation,[28-29] estimated by integrating the corresponding current transient curves obtained by CA (SI, Section S6, Figure S6a). The electrodeposited AuNPs are further characterized by performing CV experiments in a 0.5 M H_2SO_4 solution (Figure S6b),[29] The $\mathbf{Q_{ox}}$ denotes the charges related to the reduction of Au-oxides, estimated by integrating the area under the corresponding reduction peak.[28-29]

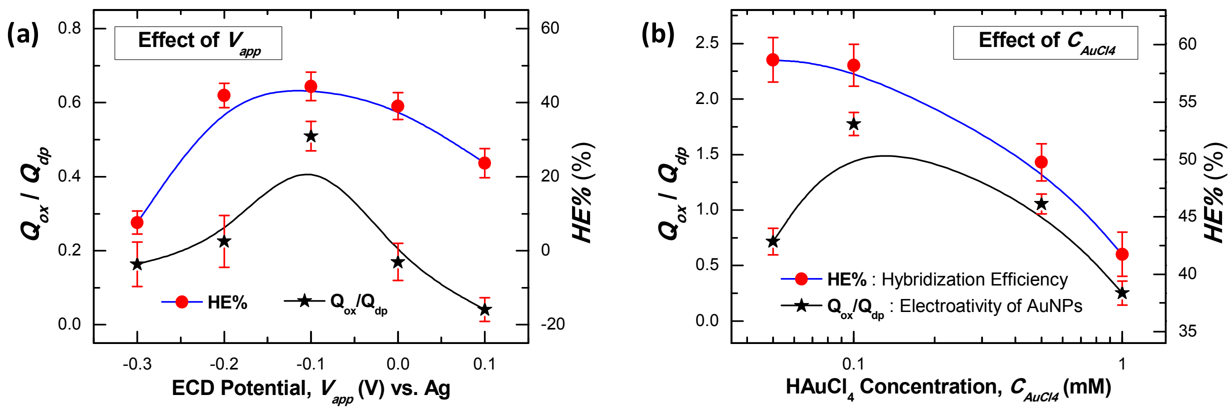

Figure 4. Electrochemical characterisations of AuNPs@MoS$_2$ electrodes. Effects of (a) applied potential (V_{app}) and (b) $HAuCl_4$ concentration ($\boldsymbol{C_{AuCl_4^-}}$) on $\boldsymbol{Q_{ox}/Q_{dp}}$ ratio and $\boldsymbol{HE\%}$. The $\boldsymbol{Q_{ox}/Q_{dp}}$ ratio represents the yield of electro-active AuNPs for the AuNPs@MoS$_2$ hybrids. The $\boldsymbol{HE\% = [(\Delta Q \times 100) / Q_{CP}]}$ represents the hybridization efficiency, where $\boldsymbol{\Delta Q = [Q_{CP\text{-}TR\text{-}AP} - Q_{CP}]}$. Error bars represent the standard deviations estimated from at least three independent measurements.

Consequently, the ratio of $\boldsymbol{Q_{ox}/Q_{dp}}$ would represent the yield of electrochemically active AuNPs electrodeposited on the MoS$_2$/SPGE. As noted by Hezard et al.,[29] the Faradaic yield for

Au electrodeposition should follow the relation: $\eta_{AuOx}/\eta_{Au} = 1.5 \times \boldsymbol{Q_{ox}}/\boldsymbol{Q_{dp}}$; the factor of 1.5 arises because 3 electrons are exchanged during Au(III) reduction, while only 2 electrons are involved in Au-oxide formation. Figures 4a and 4b demonstrate the dependence of $\boldsymbol{Q_{ox}}/\boldsymbol{Q_{dp}}$ ratio on $\boldsymbol{V_{app}}$ and $\boldsymbol{C_{AuCl_4^-}}$ respectively.

As shown in Figure 4a, AuNPs@MoS_2 hybrids electrodeposited at a high cathodic overpotential, with $\boldsymbol{V_{app}}$ = -0.1 V, exhibiting uniformly distributed, relatively monodisperse small AuNPs ($\boldsymbol{D_m} \approx$ 161 nm with $\boldsymbol{SD}$ of ±33 nm; Figure 3a), possess the highest value for the $\boldsymbol{Q_{ox}}/\boldsymbol{Q_{dp}}$ ratio. Nevertheless, it is quite surprising that the AuNPs electrodeposited at $\boldsymbol{V_{app}}$ = -0.2 V exhibit a fall on $\boldsymbol{Q_{ox}}/\boldsymbol{Q_{dp}}$ ratio, even though they possess a higher density and smaller particle size ($\boldsymbol{N_D} \approx$ 4.6 particles/μm^2, $\boldsymbol{D_m} \approx 120 \pm 30$ nm; Figure 3a) than those deposited at $\boldsymbol{V_{app}}$ = -0.1 V ($\boldsymbol{N_D} \approx$ 3.2 particles/μm^2). The lower $\boldsymbol{Q_{ox}}$, hence the lower $\boldsymbol{Q_{ox}}/\boldsymbol{Q_{dp}}$, suggests instability of the deposited nuclei. It can be deduced that the as-deposited nuclei could be rearranged, while oxidized or even dissolved back in the solution before their reduction takes place during the backward scan.

Figure 4b illustrates that the effect of $\boldsymbol{C_{AuCl_4^-}}$ on $\boldsymbol{Q_{ox}}/\boldsymbol{Q_{dp}}$ ratio. As $\boldsymbol{C_{AuCl_4^-}}$ decreases, the $\boldsymbol{Q_{ox}}/\boldsymbol{Q_{dp}}$ becomes highest at $\boldsymbol{C_{AuCl_4^-}}$ = 0.1 mM. Further reduction of $\boldsymbol{C_{AuCl_4^-}}$ (= 0.05 mM) lowers the $\boldsymbol{Q_{ox}}/\boldsymbol{Q_{dp}}$ since it suffers seriously from very low ECD-yield of AuNPs. Based on the above results the optimized Au ECD conditions of the AuNPs@MoS_2 based sensor are as follows: $\boldsymbol{V_{app}}$ = -0.1 V, $\boldsymbol{C_{AuCl_4^-}}$ = 0.1 mM and MoS_2 loading = 50 µg.

Elemental Characterisation of AuNPs@MoS_2 Hybrids. The elemental characterization of AuNPs@MoS_2 hybrids was performed via X-ray photoelectron spectroscopy (XPS), and high-resolution spectra are illustrated in Figure 5 and Figure S8 (SI, Section S7). The wide survey scan of AuNPs@MoS_2 hybrid exhibits characteristic peaks for the main elements of Mo, S and Au. In addition to those elements, the presence of C and O elements is evident, originating from the solvent and the atmosphere. Calculated from the integrated areas of respective high resolution XPS spectra, the stoichiometric ratio of Mo to S was found to be close to 1:2 (1 : 2.10 ± 0.038), demonstrating the expected MoS_2 phase.

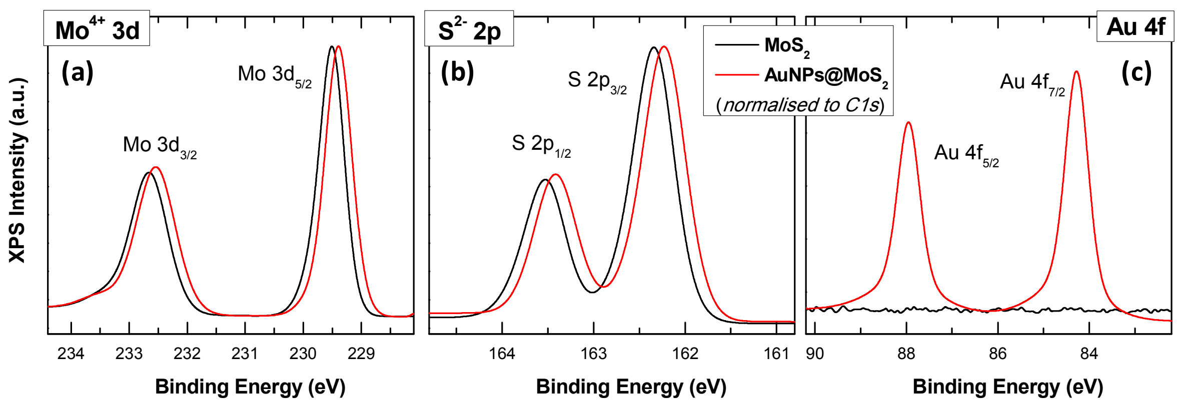

Figure 5. Elemetal characterisation of AuNPs@MoS_2 hybrids nanosheets. High-resolution XPS spectra of AuNPs@MoS_2 and pristine MoS_2 NSs drop-casted on SPGEs: (a) Mo^{4+} 3d, (b) S^{2-} 2p, and (c) Au 4f. All spectra are corrected by Shirley background and calibrated with reference to the C 1s line at 284.5 ± 0.2 eV associated with graphitic carbon. For AuNPs@MoS_2 hybrid NSs, the AuNPs is electrodeposited via CA for 360 s: V_{app}: -1.0 V. $C_{AuCl_4^-}$: 0.1 mM $HAuCl_4$ in 0.5 M H_2SO_4. MoS_2 Loading: 50 µg**.**

For AuNPs@MoS_2, the Mo 3d XPS spectrum (Figure 5a) shows doublet peaks at 229.38 and 232.53 eV attributed to Mo^{4+} $3d_{5/2}$ and Mo^{4+} $3d_{3/2}$ orbitals, respectively. Similarly doublet peaks around 162.34 and 163.53 eV, observed in Figure 5b, belong to S^{2-} $2p_{3/2}$ and S^{2-} $2p_{1/2}$ orbitals, respectively. These peak positions are indicative of Mo^{4+} and S^{2-} oxidation states in 2H phase of pristine MoS_2 NSs,[7, 36] indicating that the hybridization of MoS_2 NSs with AuNPs does not affect the crystallinity and chemical stability of MoS_2. Figure 5c shows the Au 4f spectrum, with doublet peaks positioned around 84.28 eV (Au $4f_{7/2}$) and 87.95 (Au $4f_{5/2}$), providing direct evidence for the reduction of the Au-precursors and hence the formation of AuNPs on MoS_2 NSs.[8, 36]

Interestingly, in the AuNPs@MoS_2, both Mo^{4+} and S^{2-} peaks (Figures 5a and 5b) exhibit an obvious red-shift to lower binding energies compared to that of pure pristine exfoliated MoS_2 NSs, indicating a down-shift of the Fermi level in MoS_2 due to p-type doping.[37-38] Here, the AuNPs act as a p-type dopant in MoS_2 since the $AuCl_4^-$ ions in solution can strongly withdraw electrons from MoS_2 layers and reduce to AuNPs.[23, 37-38]

Electrochemical Optimization Studies for miRNA-21 detection.

Initially the hybridization of the capture probe (**CP**) with the target miRNA sequence (**TR**), on the fabricated the AuNPs@MoS_2/SPGE platform, was confirmed by the presence of well resolved voltammograms of methylene blue redox signal, which was used an electrochemical indicator (SI, Section S8).

Optimization of RuHex Concentration (C_{RuHex}): Adsorption Isotherm of RuHex. A necessary and crucial step of the chronocoulometric detection was the determination of RuHex concentration at which the saturation condition could be achieved. At saturation condition, a complete charge compensation of the phosphate residues by redox cations was achieved i.e. one $[Ru(NH_3)_6]^{3+}$ cationic redox marker was electrostatically trapped for every three nucleotide phosphate groups.[34]

The influence of RuHex concentration (C_{RuHex}) at the **CP**-MCH-electrodes is shown in Figure 6. It is observed that the charge of surface-adsorbed RuHex, Q_{ad} in the presence of **CP**, initially increases with C_{RuHex} reaching saturation at $C_{RuHex} \geq 10$ μM on AuNPs@MoS_2/SPGEs (Figure 6a). Interestingly, at bare SPGEs, the adsorption saturation of RuHex is achieved at $C_{RuHex} \geq 40$ μM, which agrees reasonably well with the reported literature.[4, 6, 34-35, 39] The lower saturated charge values Q_{ad} at AuNPs@MoS_2/SPGEs, compared to SPGE, can be understood in terms of the lower and controlled attachment of the thiolated **CP** on AuNPs leading to a lower negative charge density.

Adsorption isotherms for RuHex, at both AuNPs@MoS_2/SPGEs and bare SPGEs in the presence of **CP**, are presented in Figure 6b, satisfying the Langmuir adsorption model[34, 39] (SI, Section S9). From the linear fitting, the saturated coverage Q_{sat} values are estimated as 1.73 and 3.68 μC, for the AuNPs@MoS_2/SPGEs and SPGE. Correspondingly, the estimated values of surface coverage density of **CP** probes ($\Gamma_{CP} = \Gamma_{DNA} = \Gamma_0(z/m)N_A$) for the **CP**-MCH-functionalized SPGE sensor agrees reasonably well with the reported values ($\Gamma_{CP} \approx 1 - 10 \times 10^{12}$ molecules/cm^2) for the shorter DNA-SAMs at the Au-electrodes.[4, 6, 34-35, 39] The 2-times higher

$\boldsymbol{Q_{sat}}$ value at the bare SPGE ($\boldsymbol{\Gamma_{CP}} \approx 3\times10^{12}$ molecules/cm^2) indicates almost 2-times higher $\boldsymbol{\Gamma_{CP}}$ values, compared to the AuNPs@MoS_2/SPGEs ($\boldsymbol{\Gamma_{CP}} \approx 1.4\times10^{12}$ molecules/cm^2).

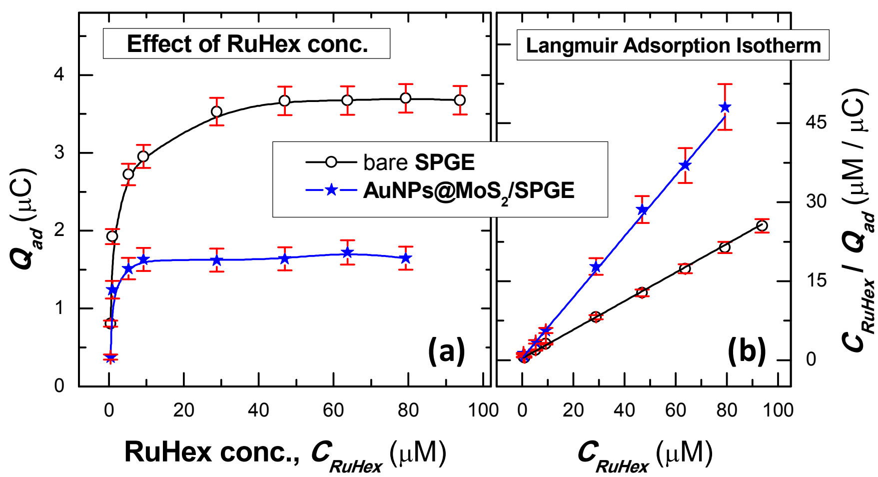

Figure 6. Effect of RuHex concentration ($\boldsymbol{C_{RuHex}}$) and **optimization of CC-detection.** (a) Adsorption isotherm of RuHex for capture DNA probe (**CP**) immobilized on bare and AuNPs@MoS_2 coated SPGEs. $\boldsymbol{Q_{ad}} = \boldsymbol{Q_{CP}} = (\boldsymbol{Q_{RuHex}} - \boldsymbol{Q_{blank}})$ and $\boldsymbol{C_{RuHex}}$ = RuHex concentration. (b) Plots of $\boldsymbol{C_{RuHex}}/\boldsymbol{Q_{ad}}$ versus $\boldsymbol{C_{RuHex}}$, demonstrating the linear fitting of the binding data to the Langmuir adsorption isotherm.

Furthermore, the linear fitting of the isotherms (Figure 6b) reveals that the association constant $\boldsymbol{K}$ of RuHex at the AuNPs@MoS_2/SPGEs (1.43 μM^{-1}) is nearly double in magnitude than that (0.83 μM^{-1}) at the bare SPGEs. The observation suggests that association of $[Ru(NH_3)_6]^{3+}$ with **CP** improves significantly at the hybrid electrode. This finding is directly related to $\boldsymbol{\Gamma_{CP}}$. At bare SPGE the high $\boldsymbol{\Gamma_{CP}}$ regimes suffer from steric hindrance, which translates into a weaker binding affinity of cationic RuHex redox complex for DNA probe. This explanation is consistent with the binding constants values reported in literature, which are either slightly weaker for dsDNA ($\boldsymbol{K}$ = 1.3 μM^{-1}) than for ssDNA ($\boldsymbol{K}$ = 2.2 μM^{-1}) or are weaker for longer length DNA compared to shorter length DNA.[34, 39-40]

Based on our results presented in Figure 6, it can be concluded that a $\boldsymbol{C_{RuHex}} \geq 10$ μM (14.5 μM was chosen) is sufficient for the CC detection of miRNA at the AuNPs@MoS_2/SPGEs, whereas for bare SPGEs-based sensors a $\boldsymbol{C_{RuHex}} \approx 50$ μM is appropriate.

Optimization of Sensing Strategies. The miRNA detection as outlined in schematic diagram in Figure 1 involves the following optimization protocols: i) electrodeposition conditions of AuNPs, ii) concentration of capture DNA probes ($\boldsymbol{C_{CP}}$), and iii) hybridization strategies of **CP** with the target miRNA (**TR**) and the signal amplified DNA probe (**AP**). Overall, the CC detection performance is defined by the hybridization efficiency ***HE%*** values, as the signature of the **CP–TR–AP** hybridization effectiveness.

Effect of Au ECD parameters. Figures 4a and 4b display the dependence of ***HE%*** value on applied potential ($\boldsymbol{V_{app}}$) and $HAuCl_4$ concentration ($\boldsymbol{C_{AuCl_4^-}}$), respectively. The effect of $\boldsymbol{V_{app}}$ on ***HE%*** follows a similar trend as the dependency of $\boldsymbol{V_{app}}$ on $\boldsymbol{Q_{ox}}/\boldsymbol{Q_{dp}}$ ratio (Figure 4a). ***HE%*** achieves the best values around the $\boldsymbol{V_{app}} \approx -0.1$ V, at which the electrodeposited AuNPs possess a small particle size ($\boldsymbol{D_m} \approx 160$ nm) with uniform distribution and a packing density ($\boldsymbol{N_D}$) of ~3.2 particles/μm^2; at the same time they provide the best yield of electrochemical activity ($\boldsymbol{Q_{ox}}/\boldsymbol{Q_{dp}}$ ratio). Figure 4b reveals that ***HE%*** improves monotonously as the $\boldsymbol{C_{AuCl_4^-}}$ decreases and reaches saturation at a concentration of 0.05 mM. On the other hand the $\boldsymbol{Q_{ox}/Q_{dp}}$ ratio attains the best value at 0.1 mM. Hence, taking into account trends for both ***HE%*** and $\boldsymbol{Q_{ox}/Q_{dp}}$ ratio, the following optimized conditions were chosen for Au ECD for the fabrication of the sensor: $\boldsymbol{V_{app}}$ = -0.1 V and $\boldsymbol{C_{AuCl_4^-}}$ = 0.1 mM, with MoS_2 loading of 50 µg.

DNA–miRNA hybridization strategy. The optimization strategy for the hybridization of **CP** with **TR** and **AP** is illustrated in the SI (Section S10 and Figure S11). The following terminology has been employed (SI, Table S3): (1) **CP** => **TR** => **AP** involves 3-steps: **CP**-immobilization followed by **CP–TR** hybridization and lastly by **TR–AP** hybridization; (2) **CP** => (**TR** + **AP**) involves 2-steps: **CP**-immobilization followed by the simultaneous hybridization of **CP** with **TR** and **AP**; and (3) **CP** => (**TR–AP**) involves 2-steps: **CP**-immobilization followed by hybridization of **CP** with previously hybridized **TR** and **AP** targets (**TR–AP**). It is clear from Figure S11 that the protocol **P#3**, **CP** => (**TR–AP**), yields the best hybridization efficiency. The ***HE%*** value improves by almost 30% compared to the sequential protocol (**P#1**).

Importance of signal amplified probe (AP). To verify the augmented function of the signal amplified probe (**AP**) in our proposed detection strategy, a miRNA-21 detection test was performed employing two different capture probes **CP** and **f-CP** (SI, Section S11 and Figure S12), with a target concentration of 10 fM. The **f-CP** probe is fully complementary to the target **TR** (Table S4) whereas **CP** is complimentary to a part of **TR** only, the remaining of **TR** is complementary to **AP**. Evidently, the 1-step hybridization of **f-CP** with **TR** (**AP#0**) cannot achieve the same hybridization efficiency, achieved by the 2-steps-protocol (**CP–TR** hybridization followed by **TR–AP** hybridization, **CP** => **TR** => **AP**). The involvement of **AP** can improve the ***HE%*** from 7% (for **AP#0**) to 10% (for **AP#3**) at the AuNPs@MoS_2/SPGE sensor. Moreover, adopting the best hybridization protocol, that involves hybridization of immobilized **CP** with previously hybridized **TR** and **AP** targets, **CP** => (**TR–AP**), as described earlier in (Section S10, Figure S11), the efficiency can be improved further to ≈17% (**AP#4**) confirming the effectiveness of the amplification probe. Furthermore, both AuNPs@MoS_2/SPGE and AuNPs@SPGE sensors, exhibit a similar trend (Figure S12), which supports enhanced impact of the signal amplified probe (**AP**).

Effect of CP concentration and hybridization time. Further optimization studies conclude that the response signal of RuHex-assisted detection could be improved by: (1) lowering concentration of **CP** (C_{CP}) and (2) optimising the time (T_H) for the hybridization of **CP** with (**TR–AP**) targets. The best values for C_{CP} are in the range of 0.3 ~ 0.1 μM. It is well known that the excessive probe DNA density (Γ_{CP}) would generate greater steric hindrance and reduce the hybridization efficiency (***HE%***). Similarly, the ***HE%*** exhibits significant improvement with the initial increase in T_H. However at much longer T_H (> 45 mins), the ***HE%*** value becomes insensitive to the T_H value.

Chronocoulometric Detection of miRNA-21.

The chronocoulometric (CC) detection of miRNA-21 at the AuNPs@MoS_2/SPGE sensor was performed as a function of target concentration (C_{TR}) employing the $\Delta Q = [Q_{CP\text{-}TR\text{-}AP} - Q_{CP}]$ and the $HE\% = [(\Delta Q \times 100) / Q_{CP}]$ as sensing parameters (Figure 7).

Two different MoS_2 NSs products (Figure 7) are compared for the fabrication of the sensor: MoS_2(1k) which consists of large and thick MoS_2 platelets (AuNPs@***MoS_2(1k)***/SPGE) and

MoS_2(10k) consisting of thin and small nanosheets (AuNPs@***MoS_2(10k)***/SPGE). A representative AuNPs-coated bare SPGE (AuNPs@SPGE) was also employed for comparison purposes.

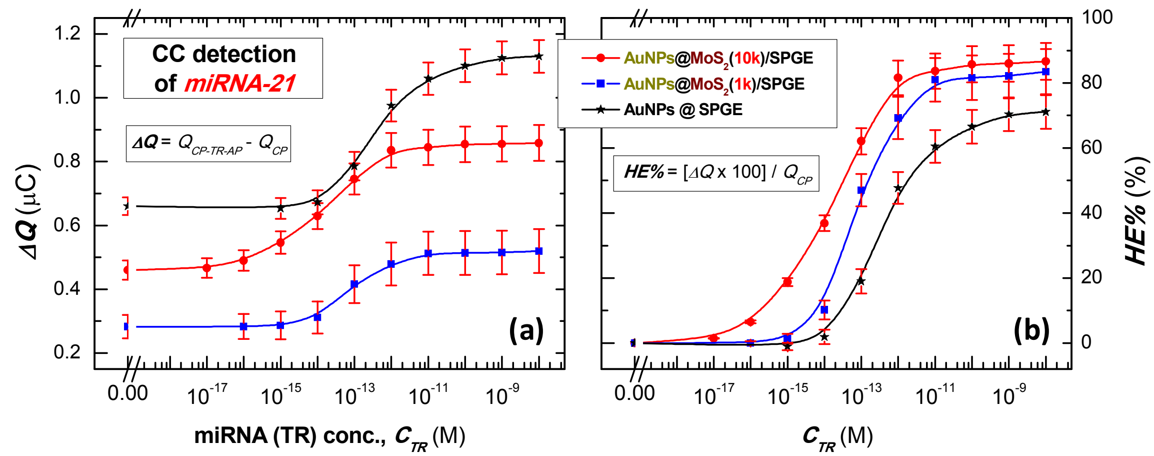

Figure 7. Chronocoulometric (CC) detection of miRNA-21. Logarithmic plot for (a) CC signal (***ΔQ***) and (b) corresponding hybridization efficiency (***HE%***) versus target miRNA (**TR**) concentration (***C_{TR}***) for the **CP**-immobilized on AuNPs (AuNPs@SPGE) and AuNPs@MoS_2 modified SPGEs employing MoS_2 nanosheets produced at centrifugation speeds of 1 k (AuNPs@***MoS_2(1k)***/SPGE) and 10 k rpm (AuNPs@***MoS_2(10k)***/SPGE).

ΔQ displays identical trends with **TR** concentration for all three sensors, exhibiting an initial rise and finally a plateau (Figure 7a). In the absence of **TR** (at ***C_{TR}*** = 0 M), relatively larger values of ***ΔQ*** are recorded at the AuNPs@SPGE sensor due to higher surface density of **CP** (***Γ_{CP}***). In contrast, both AuNPs@***MoS_2(10k)***/SPGE and AuNPs@***MoS_2(1k)***/SPGE sensors exhibit lower $\boldsymbol{Q_{CP}}$ (at $\boldsymbol{C_{TR}}$ = 0 M) because of a lower $\boldsymbol{\Gamma_{CP}}$. The misleading underperformance of the AuNPs@MoS_2/SPGE, originating from the difference in the initial $\boldsymbol{Q_{CP}}$ values (at $\boldsymbol{C_{TR}}$ = 0 M), can be avoided by employing the ***HE%*** parameter (Figure 7b).

Actually, the AuNPs@MoS_2/SPGE sensor exhibits enhanced ***HE%*** values compared to the AuNPs@SPGE sensor. Interestingly, the AuNPs@***MoS_2(10k)***/SPGE sensor possessing the more electroactive MoS_2(10k) NSs exhibits the best ***HE%*** (≈88%) followed by the AuNPs@***MoS_2(1k)***/SPGE, while the AuNPs@SPGE sensor can only achieve a ***HE%*** of 70%.

The linear regimes of the ***HE%*** (also, $\boldsymbol{\Delta Q}$) versus the logarithm of $\boldsymbol{C_{TR}}$ for the AuNPs@***MoS_2(10k)***/SPGE, AuNPs@***MoS_2(1k)***/SPGE, and AuNPs@SPGE sensors are estimated as [100 aM ~ 1 pM], [1 fM ~ 10 pM] and [10 fM ~ 10 pM], respectively. The "sensitivity" values are estimated from the linear fitting of these "linear regimes" as : 0.161 ± 0.007, 0.203 ± 0.012 and 0.203 ± 0.016 μC/log(M), respectively.

Interestingly, the AuNPs@***MoS_2(10k)***/SPGE sensor exhibits the best "experimental" limit of detection (***LoD***), of ~100 aM, followed by the AuNPs@***MoS_2(1k)***/SPGE, (***LoD*** ≈ 1 fM) and AuNPs@SPGE (***LoD*** ≈ 10 fM) sensors.

During the miRNA-21 detection study, the measurement error was estimated from the standard deviation of at least three independent experiments (n ⩾ 3), at every concentration of the miRNA target ($\boldsymbol{C_{TR}}$). The relative standard deviation (RSD), obtained for the AuNPs@MoS_2/SPGE sensors, was 8.2%, slightly higher than that of AuNPs@SPGE sensor (6.5%). The lager RSD value is believed to originate from variations in coating surface areas associated with the drop-casting process of MoS_2 NSs.

Selectivity of AuNPs@MoS_2/SPGE miRNA Sensor. To evaluate the specificity of the as-proposed AuNPs@MoS_2/SPGE sensor, the interference from non-complementary target such as miRNA-155, as well as from base mismatched strands with the same concentration (10 fM) as that of the target (miRNA-21 = **T1**) were investigated (Table S5). The study, presented in Figure 8 (SI, Section S12), clearly reveals that all 3 sensors (utilizing MoS_2(10k), MoS_2(1k), and no MoS_2 NSs) become highly sensitive in the presence of complementary target **T1**. All the sensors can also sense the single-base mismatched target (**T2**), nevertheless at considerably lower signal. The ***HE%***, measured at the AuNPs@***M-10k***/SPGE, for **T2** is only ~27% of that for **T1**, utilizing concentrations in the femtomolar range.

Interestingly, in the presence of either three-base mismatched (**T3**) or non-complementary target (miRNA-155: **T4**), no measurable signal was observed, which is a clear indication of an excellent sequence specificity of the proposed miRNA-sensor.

In the final experiment, performed in a complex medium with a mixture of all the targets (**Mix-T** = **T1+T2+T3+T4**, each target of 10 fM concentration), the AuNPs@***MoS_2(10k)***/SPGE sensor exhibits the best ***HE%*** (≈26.8%) followed by the AuNPs@***MoS_2(1k)***/SPGE (***HE%*** ≈11.4%), while the AuNPs@SPGE sensor can only achieve a ***HE%*** of ≈2.4% (Figure 8).

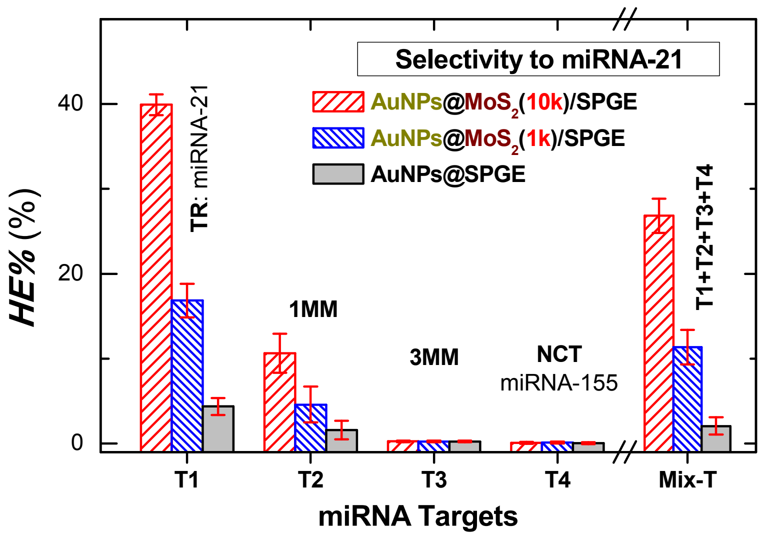

T1	Target miRNA : miRNA-21
T2	One-base mismatched miRNA-21
T3	Three-base mismatched miRNA-21
T4	Non-complementary Target : miRNA-155
Mix-T	Mixture of all miRNA targets, T1, T2, T3 AND T4

Figure 8. Selectivity of AuNPS@MoS$_2$/SPGE sensor: Hybridization Efficiency, ***HE%***, measured at the **CP**-immobilized AuNPs@MoS$_2$/SPGE and AuNPs@SPGE sensors, in the presence of: miRNA-21 (**T1: TR**); Single-base mismatched strand (**T2: 1MM**); Three-base mismatched strand (**T3: 3MM**); and the interfering non-complementary target (**NCT**) (**T4:** miRNA-155), with the same concentration of 10 fM. **CP** is the anti-miRNA-21. Error bars represent the standard deviations estimated from at least three independent measurements.

▪ CONCLUSIONS

A new simple and sensitive electrochemical platform based on AuNPs@MoS_2 hybrid nanosheets coated on commercial disposable gold screen-printed electrode (SPGEs) has been developed for the detection of miRNA-21 using a chronocoulometric (CC) approach. The work consists of two major strands: (i) the controlled synthesis and tuning of AuNPs on MoS_2 NSs via CA electrochemical deposition (ECD); and (ii) the design of a simple new bioassay involving a label free signaling amplification probe for the chronocoulometric quantification of miRNA biomarker employing the AuNPs@MoS_2 platform.

Control on AuNP density and size was achieved, by regulating the kinetics of nucleation and growth through tuning of deposition-potential ($\boldsymbol{V_{app}}$) and Au-precursor concentration ($\boldsymbol{C_{AuCl_4^-}}$). By a combination of a statistical morphological and an electrochemically activity analysis, almost monodispersed AuNPs with small size (< 90 nm) and appropriate interparticle spacing were easily accomplished on the MoS_2 NSs. The CA Au-ECD method preserved the crystalline quality of the MoS_2 NSs and induced a p-type doping.

Following the AuNP optimization study, a detailed parametric CC study was undertaken to optimize each immobilization step. Our AuNPs@MoS_2/SPGEs sensor not only improved the ***LoD*** by 2 orders (≈100 aM) but also enhanced the ***HE%*** to ≈88%, when compared to bare AuNPs@SPGEs (***LoD*** ≈ 10 fM, ***HE%*** ≈ 70%). Interestingly, the role of thin and small MoS_2 NSs was elucidated by demonstrating better sensing performance than that of thicker and larger counterparts. This work forms the first detailed and systematic study on sensitive CC detection of miRNA employing AuNPs/MoS_2 hybrids. The detection sensitivity is comparable to that obtained from systems based on complicated time consuming labelled amplification techniques. Here our design is based only on a simple non-labeled signaling probe (**AP**), which is cheap and easy to operate, avoiding complicated fabrication steps. The low detection limit originates from the controlled packing density of **CP**s, achieved by their self -assembly on AuNPs, and the intimate coupling between AuNPs and MoS_2. Our methodology provides important guidelines for the sensitive detection of miRNA cancer diagnostics.

▪ EXPERIMENTAL SECTION

Synthesis of MoS_2 Nanosheets. MoS_2 NSs were synthesized by the grinding ionic liquid assisted exfoliation method followed by size selection ultra-centrifugation steps as reported in our earlier publication.[7] MoS_2 NSs pelleted at 1000 rpm and 10,000 rpm are abbreviated as MoS_2(1k) and MoS_2(10k) respectively. MoS_2 inks were prepared by dispersing 5 mg of MoS_2 NSs in 1 ml DMF and 50 µl of Nafion solution under adequate ultrasonication.

Chronocoulometry Detection of miRNA-21. The chronocoulometry (CC) is used here as the main technique for the detection of miRNA-21, by quantifying the saturated amount of charge compensated RuHex redox marker at the hybridized electrode system (Step 6 in Figure 1). The overall principle of CC DNA detection is based on determination of surface-confined redox species like $[Ru(NH_3)_6]^{3+}$ (RuHex) at the DNA-electrode system,[1, 4, 6, 34-35, 41-42] where the cationic redox markers, RuHex, can electrostatically interact with the negative phosphate groups of the DNA or RNA. The numerical analysis of the CC data was performed through Anson plots as demonstrated in the SI (Figure S1) and described in Section S2. In a typical CC experiment the following steps were followed. At first CC was performed in blank TE buffer. From the

Anson Plot (CC-plot), which provides the measured charge (***Q***) versus the square-root of time ($t^{1/2}$), the double-layer charge term (Q_{dl}) was estimated from the y-axis-intercept ($Q_{blank} = Q_{dl}$). Next, the surface-confined redox marker, RuHex, was introduced to the TE buffer solution at a concentration that provided saturation with the probe DNA layer. The adsorption isotherm of RuHex was investigated to optimize the RuHex concentration (C_{RuHex}) and the CC-conditions. In the presence of RuHex, the y-axis-intercept of the CC-plot gave the Q_{RuHex} value. The value of surface excess of RuHex, $Q_{ad} = (Q_{RuHex} - Q_{blank}) = nFA\Gamma_0$, was calculated from the difference in the CC intercepts in the absence (Q_{blank}) and presence (Q_{RuHex}) of RuHex.

For the miRNA-detection performance study, the concentration of miRNA-21 targets (C_{TR}) was varied. For CC-based miRNA detection, the change in signal, ΔQ (= ($Q_{CP\text{-}TR\text{-}AP} - Q_{CP}$)) and the corresponding hybridization efficiency, ***HE%*** (= ($\Delta Q \times 100$) / Q_{CP}) were treated as the sensing parameters: where, Q_{CP} and $Q_{CP\text{-}TR\text{-}AP}$ represent the Q_{ad} values measured after **CP** immobilization and after its hybridization with **TR** and **AP**, respectively.

▪ ASSOCIATED CONTENT

Supporting Information

Experimental section (materials, methods and instruments, electrochemical sensing methods, synthesis of MoS_2 nanosheets, synthesis of AuNPs@MoS_2 hybrids on SPGEs, and assembly of **CP–TR–AP** on AuNPs@MoS_2/SPGE); Numerical analysis of chronocoulometric data; Effects of pretreatment of MoS_2/SPGEs and electro-deposition methods on gold nanoparticle dispersion; Equations used for the electrochemical characterizations of AuNPs and $Fe(CN)_6^{3-/4-}$ redox activity; Confirmation of sensor-fabrication strategy, via the redox characteristics of Methylene Blue (MB) detection probe; Equation deployed for the adsorption isotherm of RuHex and effect of C_{RuHex} on the voltammetric responses of RuHex; Optimization of **CP–TR–AP** hybridization strategy; Control experiment to establish the amplified function of **AP** probe; Chronocoulometric responses on **CP–TR** hybridization in absence of RuHex; and Tables presenting the sequences of oligonucleotides used in this study.

The following files are available free of charge.

▪ AUTHOR INFORMATION

Corresponding Author

*P. Papakonstantinou. E-mail: p.papakonstantinou@ulster.ac.uk.

Funding Sources

British Council, Newton fund Institutional Links, Ref: 216182787.

Notes

The authors declare no competing financial interest.

▪ ACKNOWLEDGMENTS

The authors acknowledge support from British Council (Newton fund, Institutional Links, Ref: 216182787).

▪ REFERENCES

(1) Rafiee-Pour, H.-A.; Behpour, M.; Keshavarz, M. A Novel Label-free Electrochemical miRNA Biosensor using Methylene Blue as Redox Indicator: Application to Breast Cancer Biomarker miRNA-21. *Biosens. Bioelectron.* **2016,** *77*, 202-207.

(2) Su, S.; Cao, W.; Liu, W.; Lu, Z.; Zhu, D.; Chao, J.; Weng, L.; Wang, L.; Fan, C.; Wang, L. Dual-mode Electrochemical Analysis of microRNA-21 using Gold Nanoparticle-decorated MoS_2 Nanosheet. *Biosens. Bioelectron.* **2017,** *94*, 552-559.

(3) Zhu, D.; Liu, W.; Zhao, D.; Hao, Q.; Li, J.; Huang, J.; Shi, J.; Chao, J.; Su, S.; Wang, L. Label-free Electrochemical Sensing Platform for microRNA-21 Detection using Thionine and Gold Nanoparticles Co-functionalized MoS_2 Nanosheet. *ACS Appl. Mater. Interfaces* **2017,** *9*, 35597-35603.

(4) Zhang, J.; Song, S.; Wang, L.; Pan, D.; Fan, C. A Gold Nanoparticle-based Chronocoulometric DNA Sensor for Amplified Detection of DNA. *Nat. Protoc.* **2007,** *2*, 2888-2895.

(5) Pei, H.; Zuo, X.; Pan, D.; Shi, J.; Huang, Q.; Fan, C. Scaffolded Biosensors with Designed DNA Nanostructures. *NPG Asia Mater.* **2013,** *5*, e51-n/a.

(6) Tavallaie, R.; Darwish, N.; Gebala, M.; Hibbert, D. B.; Gooding, J. J. The Effect of Interfacial Design on the Electrochemical Detection of DNA and microRNA using Methylene Blue at Low-density DNA Films. *ChemElectroChem* **2014,** *1*, 165-171.

(7) Benson, J.; Li, M.; Wang, S.; Wang, P.; Papakonstantinou, P. Electrocatalytic Hydrogen Evolution Reaction on Edges of a Few Layer Molybdenum Disulfide Nanodots. *ACS Appl. Mater. Interfaces* **2015,** *7*, 14113-14122.

(8) Wang, T.; Zhuo, J.; Chen, Y.; Du, K.; Papakonstantinou, P.; Zhu, Z.; Shao, Y.; Li, M. Synergistic Catalytic Effect of MoS_2 Nanoparticles Supported on Gold Nanoparticle Films for a Highly Efficient Oxygen Reduction Reaction. *ChemCatChem* **2014,** *6*, 1877-1881.

(9) Joensen, P.; Frindt, R. F.; Morrison, S. R. Single-Layer MoS_2. *Mater. Res. Bull.* **1986,** *21*, 457-461.

(10) Gopalakrishnan, D.; Damien, D.; Shaijumon, M. M. MoS_2 Quantum Dot-Interspersed Exfoliated MoS_2 Nanosheets. *ACS Nano* **2014,** *8*, 5297-5303.

(11) Kim, J.; Byun, S.; Smith, A. J.; Yu, J.; Huang, J. Enhanced Electrocatalytic Properties of Transition-Metal Dichalcogenides Sheets by Spontaneous Gold Nanoparticle Decoration. *J. Phys. Chem. Lett.* **2013,** *4*, 1227-1232.

(12) Dai, W.; Dong, H.; Fugetsu, B.; Cao, Y.; Lu, H.; Ma, X.; Zhang, X. Tunable Fabrication of Molybdenum Disulfide Quantum Dots for Intracellular microRNA Detection and Multiphoton Bioimaging. *Small* **2015,** *11*, 4158-4164.

(13) Oudeng, G.; Au, M.; Shi, J.; Wen, C.; Yang, M. One-Step in Situ Detection of miRNA-21 Expression in Single Cancer Cells Based on Biofunctionalized MoS_2 Nanosheets. *ACS Appl. Mater. Interfaces* **2018,** *10*, 350-360.

(14) Tuteja, S. K.; Duffield, T.; Neethirajan, S. Liquid Exfoliation of 2d MoS_2 Nanosheets and Their Utilization as a Label-Free Electrochemical Immunoassay for Subclinical Ketosis. *Nanoscale* **2017,** *9*, 10886-10896.

(15) Shuai, H.-L.; Huang, K.-J.; Chen, Y.-X.; Fang, L.-X.; Jia, M.-P. Au Nanoparticles/Hollow Molybdenum Disulfide Microcubes Based Biosensor for microRNA-21 Detection Coupled with Duplex-Specific Nuclease and Enzyme Signal Amplification. *Biosens. Bioelectron.* **2017,** *89*, 989-997.

(16) Cho, S.-Y.; Koh, H.-J.; Yoo, H.-W.; Kim, J.-S.; Jung, H.-T. Tunable Volatile-Organic-Compound Sensor by Using Au Nanoparticle Incorporation on MoS_2. *ACS Sens.* **2017,** *2*, 183-189.

(17) Nie, W.; Wang, Q.; Yang, X.; Zhang, H.; Li, Z.; Gao, L.; Zheng, Y.; Liu, X.; Wang, K. High Sensitivity Surface Plasmon Resonance Biosensor for Detection of microRNA Based on Gold Nanoparticles-Decorated Molybdenum Sulfide. *Anal. Chim. Acta* **2017,** *993*, 55-62.

(18) Huang, X.; Zeng, Z.; Bao, S.; Wang, M.; Qi, X.; Fan, Z.; Zhang, H. Solution-Phase Epitaxial Growth of Noble Metal Nanostructures on Dispersible Single-Layer Molybdenum Disulfide Nanosheets. *Nat. Commun.* **2013,** *4*, 1444-n/a.

(19) Singh, V. V.; Kaufmann, K.; de Ávila, B. E.-F.; Karshalev, E.; Wang, J. Molybdenum Disulfide-Based Tubular Microengines: Toward Biomedical Applications. *Adv. Funct. Mater.* **2016,** *26*, 6270-6278.

(20) Cai, B.; Guo, S.; Li, Y. MoS_2-Based Sensor for the Detection of miRNA in Serum Samples Related to Breast Cancer. *Anal. Methods* **2018,** *10*, 230-236.

(21) Meng, X.; Liu, Z.; Cao, Y.; Dai, W.; Zhang, K.; Dong, H.; Feng, X.; Zhang, X. Fabricating Aptamer-Conjugated Pegylated- $MoS_2/Cu_{1.8}S$ Theranostic Nanoplatform for Multiplexed Imaging Diagnosis and Chemo-Photothermal Therapy of Cancer. *Adv. Funct. Mater.* **2017,** *27*, 1605592-n/a.

(22) Su, S.; Cao, W.; Zhang, C.; Han, X.; Yu, H.; Zhu, D.; Chao, J.; Fan, C.; Wang, L. Improving Performance of MoS_2-Based Electrochemical Sensors by Decorating Noble Metallic Nanoparticles on the Surface of MoS_2 Nanosheet. *RSC Adv.* **2016,** *6*, 76614-76620.

(23) Shi, Y.; Huang, J.-K.; Jin, L.; Hsu, Y.-T.; Yu, S. F.; Li, L.-J.; Yang, H. Y. Selective Decoration of Au Nanoparticles on Monolayer MoS_2 Single Crystals. *Sci. Rep.* **2013,** *3*, 1839-n/a.

(24) Sreeprasad, T. S.; Nguyen, P.; Kim, N.; Berry, V. Controlled, Defect-Guided, Metal-Nanoparticle Incorporation onto MoS_2 Via Chemical and Microwave Routes: Electrical, Thermal, and Structural Properties. *Nano Lett.* **2013,** *13*, 4434-4441.

(25) Dunklin, J. R.; Lafargue, P.; Higgins, T. M.; Forcherio, G. T.; Benamara, M.; McEvoy, N.; Roper, D. K.; Coleman, J. N.; Vaynzof, Y.; Backes, C. Production of Monolayer-Rich Gold-Decorated 2h–Ws2 Nanosheets by Defect Engineering. *NPJ 2D Mater. Appl.* **2018,** *1*, 43.

(26) Etesami, M.; Karoonian, F. S.; Mohamed, N. Electrochemical Deposition of Gold Nanoparticles on Pencil Graphite by Fast Scan Cyclic Voltammetry. *J. Chin. Chem. Soc.* **2011,** *58*, 688-693.

(27) Finot, M. O.; Braybrook, G. D.; McDermott, M. T. Characterization of Electrochemically Deposited Gold Nanocrystals on Glassy Carbon Electrodes. *J. Electroanal. Chem.* **1999,** *466*, 234-241.

(28) Gotti, G.; Fajerwerg, K.; Evrard, D.; Gros, P. Electrodeposited Gold Nanoparticles on Glassy Carbon: Correlation between Nanoparticles Characteristics and Oxygen Reduction Kinetics in Neutral Media. *Electrochim. Acta* **2014,** *128*, 412-419.

(29) Hezard, T.; Fajerwerg, K.; Evrard, D.; Collière, V.; Behra, P.; Gros, P. Influence of the Gold Nanoparticles Electrodeposition Method on Hg(Ii) Trace Electrochemical Detection. *Electrochim. Acta* **2012,** *73*, 15-22.

(30) Penner, R. M. Mesoscopic Metal Particles and Wires by Electrodeposition. *J. Phys. Chem. B* **2002,** *106*, 3339-3353.

(31) Sheridan, E.; Hjelm, J.; Forster, R. J. Electrodeposition of Gold Nanoparticles on Fluorine-Doped Tin Oxide: Control of Particle Density and Size Distribution. *J. Electroanal. Chem.* **2007,** *608*, 1-7.

(32) Liu, X.; Li, C.; Xu, J.; Lv, J.; Zhu, M.; Guo, Y.; Cui, S.; Liu, H.; Wang, S.; Li, Y. Surfactant-Free Synthesis and Functionalization of Highly Fluorescent Gold Quantum Dots. *J. Phys. Chem. C* **2008,** *112*, 10778-10783.

(33) Zhang, J.; Wang, T.; Liu, L.; Du, K.; Liu, W.; Zhu, Z.; Li, M. Molybdenum Disulfide and Au Ultrasmall Nanohybrids as Highly Active Electrocatalysts for Hydrogen Evolution Reaction. *J. Mater. Chem. A* **2017,** *5*, 4122-4128.

(34) Steel, A. B.; Herne, T. M.; Tarlov, M. J. Electrochemical Quantitation of DNA Immobilized on Gold. *Anal. Chem.* **1998,** *70*, 4670-4677.

(35) Shen, L.; Chen, Z.; Li, Y.; Jing, P.; Xie, S.; He, S.; He, P.; Shao, Y. A Chronocoulometric Aptamer Sensor for Adenosine Monophosphate. *Chem. Commun.* **2007,** 2169-2171.

(36) Wang, T.; Liu, L.; Zhu, Z.; Papakonstantinou, P.; Hu, J.; Liu, H.; Li, M. Enhanced Electrocatalytic Activity for Hydrogen Evolution Reaction from Self-Assembled Monodispersed Molybdenum Sulfide Nanoparticles on an Au Electrode. *Energy Environ. Sci.* **2013,** *6*, 625-633.

(37) Gao, J.; Kim Young, D.; Liang, L.; Idrobo Juan, C.; Chow, P.; Tan, J.; Li, B.; Li, L.; Sumpter Bobby, G.; Lu, T.-M.; Meunier, V.; Hone, J.; Koratkar, N. Transition-Metal Substitution Doping in Synthetic Atomically Thin Semiconductors. *Adv. Mater.* **2016,** *28*, 9735-9743.

(38) Yun, J.-M.; Noh, Y.-J.; Yeo, J.-S.; Go, Y.-J.; Na, S.-I.; Jeong, H.-G.; Kim, J.; Lee, S.; Kim, S.-S.; Koo, H. Y.; Kim, T.-W.; Kim, D.-Y. Efficient Work-Function Engineering of Solution-Processed MoS_2 Thin-Films for Novel Hole and Electron Transport Layers Leading to High-Performance Polymer Solar Cells. *J. Mater. Chem. C* **2013,** *1*, 3777-3783.

(39) Li, Z.; Zhang, Z.; Cheng, G.; Yang, X.; Zhou, J.; Chen, Y. Effect of Potential Window, Concentration of Hexaammineruthenium (III) and pH on Electrochemical Quantification of Thiol-Modified DNA Monolayers on Gold. *Int. J. Electrochem. Sci.* **2014,** *9*, 4241-4250.

(40) Wong, E. L. S.; Chow, E.; Gooding, J. J. DNA Recognition Interfaces: The Influence of Interfacial Design on the Efficiency and Kinetics of Hybridization. *Langmuir* **2005,** *21*, 6957-6965.

(41) Yao, B.; Liu, Y.; Tabata, M.; Zhu, H.; Miyahara, Y. Sensitive Detection of microRNA by Chronocoulometry and Rolling Circle Amplification on a Gold Electrode. *Chem. Commun.* **2014,** *50*, 9704-9706.

(42) Zhou, L.; Wang, J.; Chen, Z.; Li, J.; Wang, T.; Zhang, Z.; Xie, G. A Universal Electrochemical Biosensor for the Highly Sensitive Determination of microRNAs Based on Isothermal Target Recycling Amplification and a DNA Signal Transducer Triggered Reaction. *Microchim. Acta* **2017,** *184*, 1305-1313.

Graphical Abstract or TOC Graphic